APPLIED OPTICS

10.1126/sciadv.1501104

Tunable light emission by exciplex state formation between hybrid halide perovskite and core/shell quantum dots: Implications in advanced LEDs and photovoltaics

Rafael S. Sanchez,[1]* Mauricio Solis de la Fuente,[1]* Isaac Suarez,[2] Guillermo Muñoz-Matutano,[2] Juan P. Martinez-Pastor,[2†] Ivan Mora-Sero[1†]

We report the first observation of exciplex state electroluminescence due to carrier injection between the hybrid lead halide perovskite ($MAPbI_{3-x}Cl_x$) and quantum dots (core/shell PbS/CdS). Single layers of perovskite (PS) and quantum dots (QDs) have been produced by solution processing methods, and their photoluminescent properties are compared to those of bilayer samples in both PS/QD and QD/PS configurations. Exciplex emission at lower energies than the band gap of both PS and QD has been detected. The exciplex emission wavelength of this mixed system can be simply tuned by controlling the QD size. Light-emitting diodes (LEDs) have been fabricated using those configurations, which provide light emission with considerably low turn-on potential. The "color" of the LED can also be tuned by controlling the applied bias. The presence of the exciplex state PS and QDs opens up a broad range of possibilities with important implications not only in tunable LEDs but also in the preparation of intermediate band gap photovoltaic devices with the potentiality of surpassing the Shockley-Queisser limit.

INTRODUCTION

Hybrid halide perovskites (PS) are probably the hottest current material on photovoltaics with a record certified power conversion efficiency (PCE) of 20.1% (*1*). Furthermore, this efficiency record has been reached in just a few years after the first reports of PS-based liquid solar cells in 2009 (*2*) and the important breakthrough of the development of all-solid state devices in 2012 (*3*, *4*). In addition, incredibly outstanding efficiencies have been reported for devices fabricated by using solution processing techniques giving rise to polycrystalline films and hence using very low cost methods. All these facts have boosted interest for this family of materials with a general formula ABX_3 (A = organic cation, B = metallic cation, and X = halide anion, where $CH_3NH_3PbI_3$ has been the most extensively studied). Moreover, the excellent electro-optical properties of PS and its high photoluminescence quantum yield (PLQY) (*5*) have also piqued interest for the development of light-emitting diodes (LEDs) (*6*–*8*) and lasers (*5*, *9*, *10*). To explore the full potential of PS, the combinations with different organic and inorganic materials, mainly playing the role of selective contacts (*11*), have been broadly tested. Here, we report the first observation of light emission associated to PS/quantum dot (QD) exciplex (charge transfer) state. This is an important proof of concept that opens a broad range of potentialities and paves the way to new and advanced optoelectronics. Its main advantages include easy tuning of electroluminescence (EL) emission by controlling the QD size and efficient pumping not only by optical excitation but also by electrical injection.

The interaction among materials of different nature can produce interesting synergies that might be beneficial, not only by improving a feature but also by giving rise to new properties or phenomena yet to be seen in single materials. QDs are a family of materials with very interesting properties from an optoelectronic point of view, including the easy tunability of their band gaps (*12*) (simply by controlling particle size within the exciton confinement limit) that confers to these systems excellent properties for the development of solar cells (*13*, *14*) and LEDs (*15*). Despite the clear interest in both families of materials (PS and QDs), there are relatively few papers in which interactions of both systems are presented, mainly based on using PS as the capping agent of QDs (*16*, *17*). Very recently, Sargent and co-workers have published an outstanding study (*18*) that reports the preparation of polyheterocrystalline solids with PbS QDs embedded in a $CH_3NH_3PbI_3$ matrix. The PS and QDs used (effective band gap around 1 eV) form a type I junction, thus significantly enhancing the photoluminescence (PL) quantum emission in comparison with a simple QD layer or with QDs embedded in an alternative NaI Matrix. Here, we move one step further. We have analyzed the interaction between PS and core/shell QDs of different sizes, but smaller than the ones used in a previous study (*18*) to promote a type II junction. This alignment gives rise to a PS/QD exciplex state observed not only by optical pumping but also by electrical injection. This proof of concept could have huge implications not only in the development of advanced LEDs, as demonstrated here, but also for intermediate band gap (IB) solar cells (*19*, *20*) with the potentiality of surpassing the Shockley-Queisser (SQ), which we discuss briefly as an interesting potential implication of the results reported here.

RESULTS AND DISCUSSION

We have prepared single layers of $MAPbI_{3-x}Cl_x$ PS and core/shell PbS/CdS colloidal QDs (see Fig. 1A). Despite the amount of Cl being very low, we used the most common nomenclature in the literature for the $MAPbI_3$ PS synthesized using a $PbCl_2$ precursor (*3*) to clearly identify the synthesis process that has important implications in the final

[1]Institute of Advanced Materials (INAM), Universitat Jaume I, 12006 Castelló, Spain. [2]UMDO, Instituto de Ciencia de los Materiales, Universidad de Valencia, 46071 Valencia, Spain.
*These authors contributed equally to this work.
†Corresponding author. E-mail: sero@uji.es (I.M.-S); Juan.Mtnez.Pastor@uv.es (J.P.M.-P)

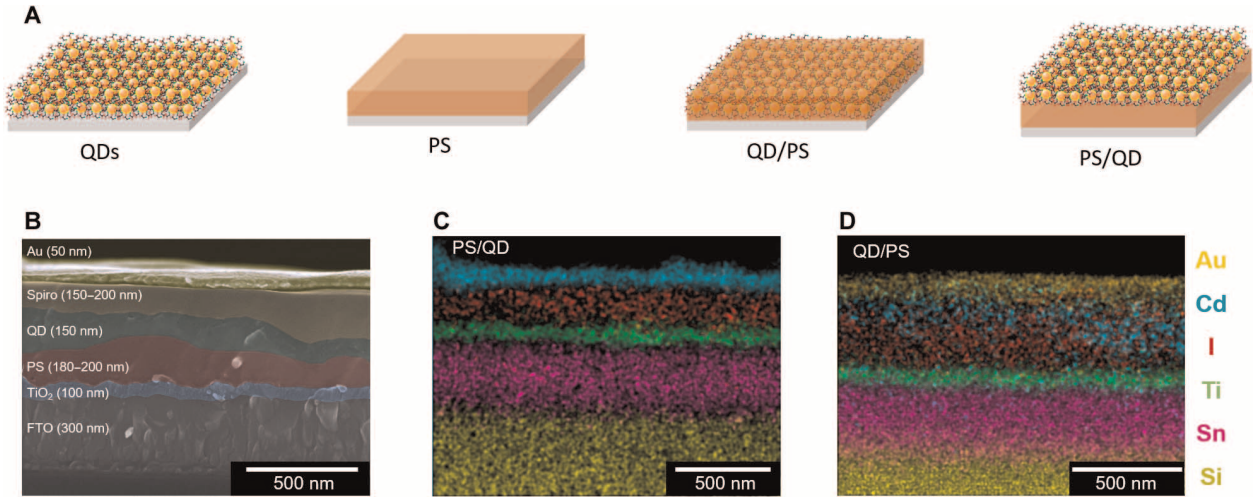

Fig. 1. Schemes, SEM, and EDX mapping of the prepared samples. (**A**) Schemes of the samples analyzed in this study formed by single layers of PS and QDs and bilayers of QD/PS and PS/QDs. Two types of QDs with different particle sizes (2.3 and 3 nm) have been analyzed in this study. (**B**) SEM picture of the cross section of a PS/QD complete device. The picture has been taken using backscattered electrons to enhance the contrast between different layers. The image contrast is increased by using colors for the different layers. The average thickness of each layer is also indicated. A thin layer of 300 nm of transparent conduction SnO_2:F (FTO) on glass is used as a substrate. TiO_2 and spiro-OMeTAD act as electron- and hole-injecting layers, respectively, and core/shell PbS/CdS 3 nm and the PS bilayer act as the electroluminescent layer. (**C**) Elemental mapping obtained by EDX for a 3-nm PS/QD sample. (**D**) Elemental mapping obtained by EDX for a 3-nm QD/PS sample. Si, Sn, Ti, and Au allow the identification of glass, FTO, TiO_2, and Au contact layers, whereas I and Cd allow the identification of PS and QD layers.

performance. Core/shell QDs have been chosen because the presence of the shell notably increases the PLQY (20% versus 1% for core PbS QDs in hexane solution) (*21*). The enhancement of PLQY has important implications in the performance of both visible (*15*) and infrared (IR) (*21*) QD LEDs. In addition, bilayers of QDs/PS and PS/QDs (see Fig. 1A) have been prepared, with the aim of exploiting the unexplored synergies between PS and QDs. The preparation of bilayers has special requirements depending on the deposition sequence (more details about preparation of samples and devices can be found in Materials and Methods). The different samples have been prepared on an insulating glass substrate and on a transparent conductive glass with SnO_2:F (FTO) to prepare LEDs. For LEDs, TiO_2 has been deposited on the FTO as an electron injection layer, whereas spiro-OMeTAD was used as a hole-injecting layer. We have recently proven that this combination of charge-injecting contacts can be used for the preparation of efficient PS-based LEDs (*7*). The PL and EL have been systematically characterized for the different samples, allowing us to observe the presence of an exciplex state with easily tunable emission by controlling the QD crystal size.

QD layers have been prepared by a single spin-coating cycle of a QD solution followed by a ligand exchange process to replace the original oleic acid (OA) capping by the shorter mercaptopropionic acid (MPA). Two different PbS/CdS core/shell QD sizes have been used in this experiment: 2.3 and 3 nm in diameter. The choice of MPA is based on our previous work (*21*), wherein we showed that the MPA was the ligand that produces higher external quantum efficiencies in PbS/CdS QD LEDs in comparison to other ligands also analyzed in that study, namely, thioglycolic acid, 1,2-ethanedithiol, and ethylenediamine. Figure 1B exhibits a cross section of a 3-nm PS/QD indicating the average thickness of the different layers. Scanning electron microscopy (SEM) pictures of the surface of the different layers are depicted in fig. S1. Figure 1 (C and D) shows the compositional mapping obtained by energy-dispersive x-ray (EDX) microanalysis. It can be clearly observed that whereas PS/QD produces a clear bilayer, there is penetration of PS into the colloidal QD layer in QD/PS samples, thus producing an intermixed layer due to PS infiltration. The different nature of both bilayers is shown in the schemes in Fig. 1A. SEM pictures of the surface also point in the same direction (see fig. S1).

After thin-film deposition and ligand exchange, the two different PbS/CdS core/shell QD sizes used in this experiment (2.3 and 3 nm in diameter) give rise to PL bands centered at 820 and 920 nm, respectively (see Fig. 2A). The PL of the QD layer is slightly red-shifted, compared to the PL in solution, after film deposition and ligand exchange (fig. S2). The single layer of PS exhibits a PL peak at 774 nm (see the black line in Fig. 2B). The PL obtained for the PS/QD and QD/PS samples with 3-nm QDs is also represented in Fig. 2B (results for the 2.3-nm QDs are similar and are plotted in fig. S3). Note that for the bilayer samples, the PL from both QD and PS is strongly quenched. Quenching of PL for both peaks points to a type II alignment between PS and both kinds of QDs, as it is schematically represented in Fig. 2C. Photogenerated holes in PS can be transferred to the QDs, whereas photogenerated electrons in the QDs can be transferred to the PS, as indicated by the dashed arrows in Fig. 2C, thus producing the quenching of individual PL bands associated to direct exciton recombination at PS and QDs (Fig. 2B). This type II alignment is also in qualitative agreement with the corresponding conduction band (CB) and valence band (VB) energy values reported and/or extrapolated from literature (*4*, *22*, *23*) (fig. S4).

However, the most interesting feature is observed deeper in the IR (see Fig. 2D). For PS single layers (Fig. 2B), only a PL peak corresponding to the direct CB-to-VB recombination (solid arrow 1 in Fig. 2C) is observed. As expected, no PL has been measured in the 900- to 1700-nm range for the PS samples (black line in Fig. 2D). In the same way, for the QD single layers, only the low-energy PL tail of the exciton recombination band (solid arrows 2 and 3 in Fig. 2C) is observed in this

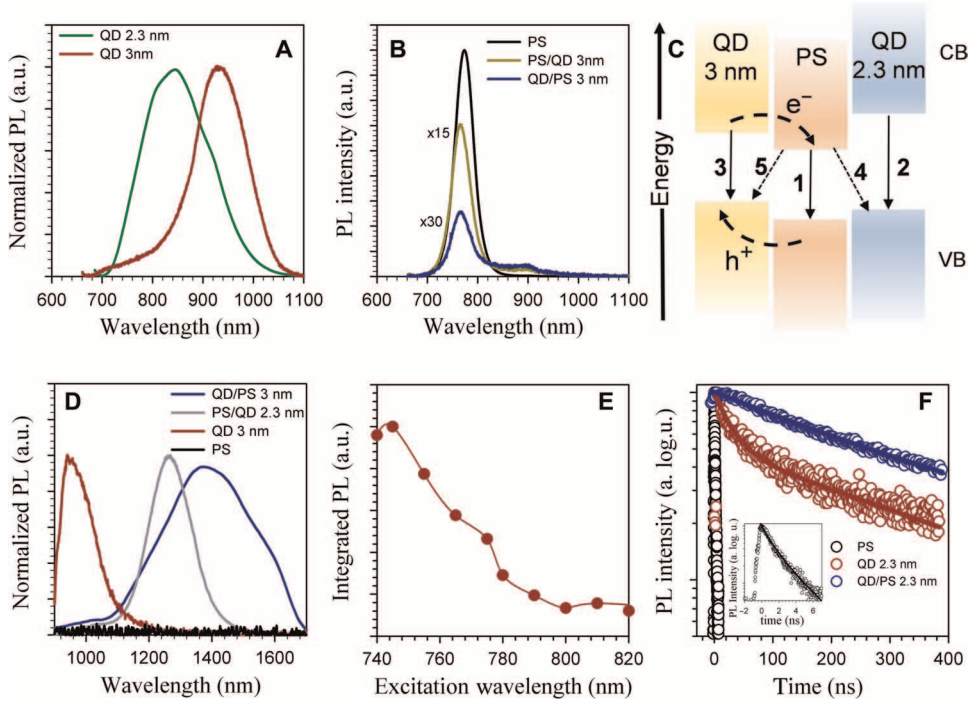

Fig. 2. PL study of single-layer and bilayer samples of PS and core/shell PbS/CdS QDs. (**A**) PL of a thin layer of QDs using two QD sizes: 2.3 and 3 nm. a.u., arbitrary unit. (**B**) PL of PS single layer and from bilayers using 3-nm QDs (for 2.3-nm QDs, see fig. S2); PL from PS/QD was multiplied by a factor 15, whereas PL from QD/PS was multiplied by a factor 30, for an easier comparison. (**C**) Proposed relative energy diagram of PS and both kinds of QDs analyzed in this study. Relative positions of CB and VB are in agreement with literature predictions (fig. S3). Solid arrows 1, 2, and 3 indicate the band gap emissions from PS, 2.3-nm QD, and 3-nm QD, respectively. Dotted arrows 4 and 5 indicate the exciplex emission of samples prepared with PS + QD 2.3 nm and PS + QD 3 nm, respectively. Dashed arrows indicate charge transfer processes of electrons, e^-, and holes, h^+, between PS and QD 3 nm (analogous processes, not represented, should be expected for 2.3-nm QDs), causing the PL quenching of bilayers. (**D**) PL recorded using an InGaAs detector at the IR region between 900 and 1700 nm. (**E**) PL excitation spectra, around the PS band gap, of the exciplex PL band (integrated) in the QD/PS bilayer with 3-nm QDs. (**F**) TRPL spectra recorded at the PL peak of PS, QD, and QD/PS samples for 2.3-nm QDs (open symbols) and exponential fitting (solid lines) using a single exponential decay (QD/PS bilayer) or a double exponential decay (PS and QD single layers). Inset, TRPL of the PS layer. a. log. u., arbitrary logarithmic unit.

IR region limited by the detector (brown line in Fig. 2D). Nevertheless, a new PL band is observed for bilayer samples (1400 nm for 3-nm QDs and 1240 nm for 2.3-nm QDs; blue and gray lines in Fig. 2D) due to the QD band gap and its alignment to that of PS, as argued above. A lower PL intensity has been detected for the QD/PS configuration in comparison to PS/QD (see fig. S5). The PL excitation spectrum of the IR PL band in the PS/QD sample with 3-nm QDs (Fig. 2E) clearly shows an increase of intensity for wavelengths at the PS absorption band edge. These facts indicate that although PS plays an active role in the emission process for the bilayer sample configuration, the IR emission signal is not exclusively due to PS. Taking into account the shift of the peak with the QD size as well, it is straightforward to conclude that peaks observed in Fig. 2D are produced by the synergistic interaction of PS and QDs. Consequently, an exciplex state involving states from both PS and QDs is formed, and it can be detected by PL emission (dotted arrows 4 and 5 in Fig. 2C). It is interesting to highlight that for the observation of such kind of state, a more intimate contact between both materials is commonly required, for example, CdSe QDs embedded in CdTe quantum rods (*24*) or blend organic layers (*25*). However, MPA QD capping hinders a perfect close contact at the boundary between PS and QDs. In this sense, a strong interaction can be inferred between PS and QDs, and/or a certain role of the capping agent in the exciplex state formation cannot be ruled out. It is also noteworthy that for the PS/QD configuration, an abrupt interface between PS and QDs is observed (Fig. 1C); however, for the QD/PS samples, the PS solution infiltrates the QD layer (Fig. 1D), producing a red shift observed for the QD luminescence peak position (fig. S6). The growth of PS on top of the QD layer also produces a small blue shift of the PS PL peak (see Fig. 2B and fig. S6). This shift could be attributed to a decrease of the PS grain size (*26*, *27*), which is in agreement with the observed PS infiltration scenario.

Time-resolved photoluminescence (TRPL) experiments have been performed to determine the characteristic decay times of PS, QD, and exciplex PL emission. Figure 2F shows the TRPL spectra for their corresponding optical transitions (open symbols). PS (inset in Fig. 2F) exhibits a very fast decay that can be fitted (solid lines) considering two decay times of 1.1 ± 0.1 and 3 ns. The exciton recombination in the QD (2.3 nm) single layer is also characterized by two decay times of 30 ± 5 and 400 ns, with the short one attributed to the exciton lifetime and the long one attributed to carrier recombination through traps or surface states (*28*). Conversely, only a single lifetime, 310 ± 20 ns, is deduced for the QD/PS (2.3 nm) bilayer, thus highlighting the different nature of the exciplex state in comparison to those in direct band gap semiconductors, PS and QDs. Such a long recombination time is consistent with our interpretation for the type II band alignment between the PS and QD layers, giving rise to a PS/QD spatially indirect carrier recombination, as occurs in most known III-V heterostructures (*29*). Moreover, considering the PS decay time extracted from Fig. 2F and the ratio between PL observed with an excitation wavelength below

the PS band gap (740 nm) and above the PS band gap (110 nm), the injection time of the hole from PS into the QD should be at least lower than 1 ns (PL decay time for PS sample) and can be roughly estimated in the order of 100 ps (see fig. S7 for further discussion).

Apart from the fundamental interest that arises from the observation of the PS/QD exciplex state between two materials of different nature, there is also a huge applied interest. This exciplex state may give rise to important and unprecedented practical applications pointing to the development of new optoelectronic devices. To explore these implications, LEDs with different active layer configurations (see Fig. 1A) have been prepared using compact TiO_2 and spiro-OMeTAD as electron- and hole-injecting layers, respectively (see Fig. 1B). Figure 3A shows the EL of a QD/PS (3 nm) sample under a different applied bias. A sharp rise in current is observed in *J-V* curves (fig. S8) for all the prepared devices associated to the diffusion current (*30*). Transport properties of the bilayer are governed by the PS, whereas the single QD layer presents a significantly higher resistivity (fig. S8).

Two peaks are observed in Fig. 3A corresponding to PS and QD band gap emission. The EL from QD is red-shifted in the bilayer samples due to the interaction with PS (fig. S9), as it has been previously discussed for PL measurement. The relative intensity of both peaks has a strong dependence with the applied bias, V_{app}; consequently, the "color" of the emitted light depends on it. The relative weight of the PS and QD emission signals depends on the bilayer configuration. Figure 3B shows the EL at a different applied bias for the 2.3-nm PS/QD. A comparison for the PS/QD configuration between samples fabricated with 2.3 and 3 nm is depicted in fig. S10. For the PS/QD configuration, the weight of QD emission on the total emission is higher than that in QD/PS bilayers (Fig. 3A and fig. S10). This behavior is due to the higher conductivity of PS and the infiltrated configuration of QD/PS (Fig. 1D) in contrast to the sharp interface present in PS/QD samples (Fig. 1C). Consequently, in infiltrated QD/PS samples carriers can just move through the PS while in PS/QD samples they have necessarily to move through the QD layer increasing the weight of QD EL in this last case. Once the density of injected carriers increases significantly with the applied voltage, the PS emission starts to increase. The inset in Fig. 3 (A and B) shows the ratio between PS and QD EL intensities. This ratio follows a linear behavior with V_{app}, thus allowing an easy control and tunability of the LED color just by changing the applied voltage. The slope of the linear regressions depends strongly on the configuration and QD size. The slope for 3-nm QD/PS is 0.5 V^{-1} (inset in Fig. 3A), whereas for the 2.3-nm PS/QD, it is 0.06 V^{-1}, which is one order of magnitude lower (inset in Fig. 3B).

The bilayer LEDs present lower external quantum efficiency (EQE) than their single-layer (PS or QD) counterparts (fig. S11). Nevertheless, it is important to remark that the EQE of the bilayer devices is underestimated, because only the EL from the PS and QD band gap transitions (Fig. 3A) is considered (not the emission from the exciplex state). The EL emission from the PS/QD exciplex state at a different applied bias for the PS/QD (2.3 nm) sample is depicted in Fig. 3C. The EL peak intensity is linearly proportional to the V_{app} (see Fig. 3C, inset). It is a remarkable fact that the exciplex state could be electrically pumped in such simple configurations with a clear signature at voltages as low as 1 V and with an extrapolated turn-on potential as low as 0.77 V. Therefore, the emission from the exciplex state is observed at a voltage lower than the value of E_G/e for both PS and QDs, where e is the elementary charge. Consequently, the color of the emitted light at low enough applied voltage corresponds exclusively to the exciplex state wavelength that can be tuned by the size of QDs (as well as potentially influenced by the kind of PS used). In the concrete case of the exciplex state with 1300-nm emission (see Fig. 3C), it could have interesting applications in the second window of telecommunications. Extrapolation to visible range emission in the case of LEDs is envisaged by using PS and QDs with wider band gaps. This concept would allow the realization of tunable color LED switching, for example, between IR and visible range just by changing V_{app}. In addition, there is plenty of room for optimization because the configurations used here for the proof-of-concept demonstration are intentionally simple for experimental clarity reasons, thus minimizing the number of layers and using planar configurations.

IMPLICATIONS

Furthermore, extremely important implications for advanced photovoltaics could be predicted. Because of the reciprocity principle, if an electron and hole from an exciplex state can recombine to produce a photon, the reciprocal process in which a photon can produce an electron-hole pair at the exciplex state is also possible. This fact opens the possibility of a new implementation of the IB concept, thus taking benefit from the PS

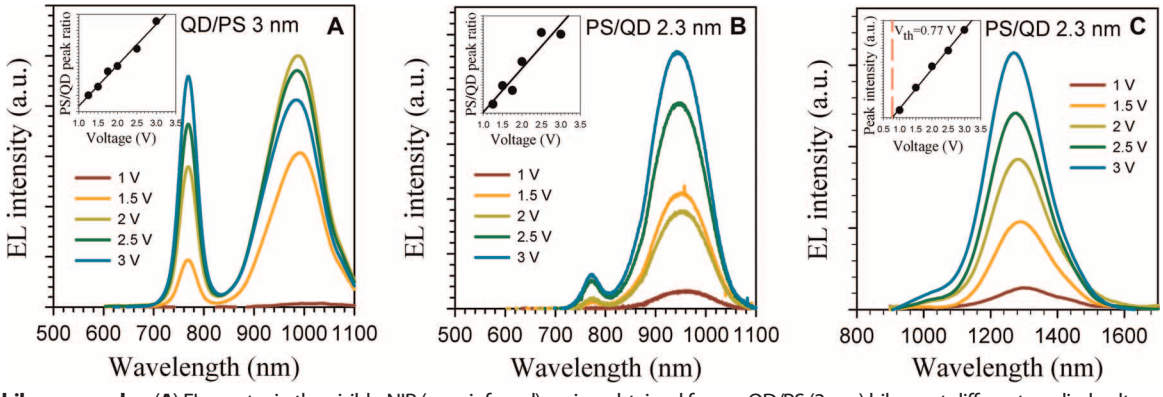

Fig. 3. EL of bilayer samples. (**A**) EL spectra in the visible-NIR (near infrared) region obtained from a QD/PS (3 nm) bilayer at different applied voltages. Inset, EL PS/QD peak intensity ratio as a function of the applied voltage of the same sample. (**B**) EL spectra in the visible-NIR region obtained from a PS/QD (2.3 nm) bilayer at different applied voltages. Inset, EL PS/QD peak intensity ratio as a function of the applied voltage of the same sample. (**C**) EL spectra in the IR region obtained from a PS/QD (2.3 nm) bilayer at a different applied bias. Inset, EL peak intensity as a function of the applied bias (solid symbols); the black solid line corresponds to the linear fit, and the red dashed line indicates the extrapolated threshold turn-on potential, V_{th}.

and QD synergies. In a conventional solar cell, the maximum PCE is limited not only because solar cells cannot absorb photons with energy lower than the absorber E_G but also because of the limited exploitation of photons with energy higher than E_G; only an energy equivalent to E_G can be used because the energy in excess is quickly lost as heat by thermalization. Tandem configuration has been used to surpass this limitation. However, IB is an already known concept for surpassing the SQ limit in a more efficient way than the tandem devices approach (*19*). IB approach consists in the utilization of one or several IBs in the band gap of a semiconductor with bandgap, E_G (see Fig. 4). IBs would act as stepping stones, thus allowing low-energy photons to transfer electrons from VB to CB by the absorption of a couple of photons with energies E_H and E_L (processes 2 and 3 in Fig. 4). The optimum exploitation of this mechanism can boost the maximum theoretical efficiency of a photovoltaic device to 63% under high concentrated light (*20*).

Different configurations have been proposed for IB solar cells including the use of the confined states in a QD as IB (*31*). Such kind of configuration has demonstrated a slight photocurrent enhancement due to sub–band gap photon absorption in a crystalline GaAs matrix with InAs self-assembled QDs (*32*). However, the PCE of IB cells did not surpass the efficiency of the cell without QDs because it was limited by the low density of QDs; an increase of the layers containing QD produces a strain accumulation that severely degrades cell performance. Here is where the PS/QD exciplex state exhibits its full potential to produce IB solar cells. Polycrystalline PS could remove the strain limitation, because it is relaxed at the grain boundaries. The versatility of PS and QDs also allows an appropriated design of the system to work at optimum conditions (*20*).

CONCLUSIONS

In summary, we have observed for the first time the emission from the PS/QD exciplex state by using $MAPbI_{3-x}Cl_x$ PS and core/shell PbS/CdS QDs. Our approach constitutes a valuable proof of concept on the coupling of two important families of materials for the development of optoelectronic devices, hybrid halide PS and solar cells. The emission of the exciplex state can be easily tuned by controlling the size of QDs. This proof of concept has been demonstrated by using optical pumping and electrical injection.An electrically pumped exciplex state opens a highly interesting scenario for the development of new and advanced optoelectronic devices. We have succeeded in preparing LEDs with color tunability depending on the applied voltage. At low enough V_{app}, only the emission from the exciplex state is observed, because it presents a turn-on voltage lower than the E_G/e of both PS and QDs. At higher V_{app}, the LED color was still easily tuned with a PS/QD PL intensity ratio following a linear behavior as a function of the applied bias. Moreover, exciplex states could also have important implications for the development of advanced photovoltaic devices with the potentiality of surpassing the SQ limit by refreshing the IB solar cell concept. The use of PS could have important advantages in comparison to previous approaches for IB cells due to the benign defect physics of PS (*33*), which allows high-efficiency photovoltaic devices with polycrystalline samples and an easy relaxation of strain induced by the presence of QDs. Therefore, the synergy between PS and QD based on the exciplex state reported here is envisaged to have important repercussions on the development of advanced optoelectronic devices.

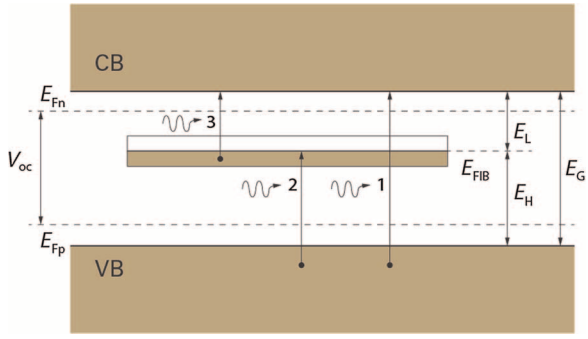

Fig. 4. Implications for advanced photovoltaics. Energetic diagram of an IB photovoltaic device, adapted from Luque and Martí (*19*) and Luque *et al.* (*20*). In an IB system, one or more levels in the band gap, E_G, of a semiconductor that are not contacted by the extraction contacts exist. Consequently, the open-circuit potential, $V_{oc} = E_{Fn} - E_{Fp}/e$, is still determined by the Fermi level splitting of electron and holes, E_{Fn} and E_{Fp}, respectively, associated with the occupation of the CB and VB, as in a single absorber photovoltaic system. However, in contrast with conventional systems, it is possible to define a Fermi level of the intermediate band gap, E_{FIB}, situated at energetic distances E_L, from the bottom of CB, and E_H, from the top of VB. This isolated IB produces that in addition to photons with energy equal to or higher than E_G (process 1), it is also possible to harvest photons with energy lower than E_G due to photon absorption through this IB state (processes 2 and 3).

MATERIALS AND METHODS

PbS/CdS QD synthesis

Core/shell QDs were synthesized according to procedures previously reported (*21*). Briefly, for the synthesis of 3-nm PbS nanocrystals, PbO (0.9 g), OA (2.7 g), and 1-octadecene (ODE; 36 ml) were loaded in a three-necked round-bottom flask (RBF) connected to a Schlenk line, and the solution was heated up to 150°C under nitrogen for a complete formation of Pb-oleate moieties. The mixture was degassed for 30 min under vacuum, and 3 ml of trioctylphosphine (90%) was injected. The reaction flask was allowed to cool down to 110°C, and a solution of hexamethyldisilathiane (HMDS) was swiftly injected (0.420 ml of HMDS in 4 ml of anhydrous ODE). The temperature was gradually decreased to 30°C, and the reaction product was washed with ethanol/acetone (1:1, v/v) three times, centrifuged (3000 rpm, 10 min), and dispersed in toluene.

For the growth of the CdS shell, CdO (0.34 g), OA (1.85 g), and ODE (40 ml) were introduced in a three-necked RBF, and the dispersion was heated at 220°C for 2 hours in air and degassed at 150°C for 1 hour. The as-prepared PbS QDs solution (100 mg/ml, 5 ml) was swiftly injected at 70°C. After 5 min of reaction, the temperature was decreased by adding the nonsolvent mixture (ethanol/acetone, 1:1, v/v). The same washing steps as for the PbS nanocrystals were used for the PbS/CdS QDs. An identical procedure was applied for the synthesis of 2.3-nm PbS QDs; however, 2 g of OA was used for PbS core formation, and 0.34 g of CdO and 1.85 g of OA were used for the growth of the CdS shell.

TiO_2 compact layer

FTO substrates were cleaned with soap, sonicated in a mixture of acetone/ethanol (1:1, v/v) for 15 min, and treated with a UV (ultraviolet)–O_3 lamp for 15 min. The TiO_2 compact layer was deposited by spray pyrolysis at 450°C, consuming 40 ml of a solution of titanium di-isopropoxide bis

(acetylacetonate, 75% vol. 2-propanol) in ethanol (1:39, v/v); the films were sintered at 450°C for 30 min.

PS/QDs sample

The mixed halide PS $CH_3NH_3PbI_3$ was prepared as described previously (*7*). The precursor solution was prepared by dissolving 0.423 g of CH_3NH_3I and 0.246 g of $PbCl_2$ (3:1 molar ratio, respectively) in 1 ml of anhydrous *N*,*N*-dimethylformamide at room temperature. The PS precursor solution was deposited by spin coating (4000 rpm, 60 s) on TiO_2 substrates, followed by a thermal treatment at 100°C for 30 min and annealing in air at 100°C for 1 hour. After the samples were prepared, a layer of PbS/CdS QDs (150 mg/ml) was deposited by spin coating (2500 rpm, 10 s). After depositing the QD layer, the film was treated with a solution of MPA (1.3 M in 2-propanol) for the ligand exchange, and the excess ligand was removed by spin coating (2500 rpm, 10 s) and adding an excess of 2-propanol. The hole transport layer (HTL) was deposited via spin coating (4000 rpm, 30 s); using 100 µl of a solution of 59 mM spiro-OMeTAD [2,2,7,7-tetrakis(*N*,*N*-di-*p*-methoxyphenylamine)-9,9-spirobifluorene] in chlorobenzene adding as additives 17.3 µl of 4-*tert*-butylpyridine and 10.5 µl of a solution of bis-(trifluoromethylsulfonyl)amine lithium salt in acetonitrile (520 mg/ml). Gold electrodes (60 nm thick) were thermally evaporated under a vacuum of 3×10^{-6} mbar at a rate of 0.1 Å s^{-1} during the first 10 nm and after 1 Å s^{-1}.

QD/PS sample

The stock solution of QDs (150 mg/ml) was deposited onto the TiO_2 film (2500 rpm, 10 s); once deposited onto a layer, the exchange of ligand was realized with 1.3 M MPA in methanol, followed by washing with methanol and octane to remove the excess ligand. $CH_3NH_3PbI_3$ PS solution was deposited by spin coating (4000 rpm, 60 s) followed by a thermal treatment at 100°C for 60 min inside the glove box. It was verified that standard annealing on air atmosphere significantly reduced device performance. The HTL and the gold electrodes were deposited as described previously.

Characterization of samples in solution, on film, and on devices

The surface morphology of the films was obtained by SEM (JEOL 7001F-FEG-SEM). SEM images were realized with a SEM-FEG Hitachi S-4800 microscope. Absorbance and PL spectra in solution and on a film were measured using a spectrophotometer CCD (charge-coupled device) detector (Andor iDUS DV 420A-OE) coupled with a spectrograph as a diffraction grating (Newport 77400). The excitation source for PL was a commercial red laser diode (650 nm), and a glass filter (FGL715S) was placed at the detector entrance to cut-off the excitation light. A stabilized tungsten-halogen light source (SLS201, from Thorlabs) was used for absorbance measurements.

The PLQY values of the QDs were measured in hexane ($\lambda_{exc} = 650$ nm) by the comparative method using the commercial dye IR125 as the emission reference (PLQY = 0.043 in methanol). All the solutions showed an absorbance below 0.1 U at the excitation wavelength to avoid PL autoabsorption, self-quenching, and related interactions.

EL and current density–voltage (*J*-*V*) curves were obtained using a previously described equipment synchronized to a potentiostat (Gamry Reference 3000). The measurements were realized under dark conditions under nitrogen N_2 flow at room temperature.

PL experiments at IR wavelengths (900 to 1700 nm) were carried out by pumping the samples with a Ti:Sapphire (Coherent Mira 900D) mode locked laser at an operation wavelength tuned between 740 and 820 nm. The backscattered PL signal was dispersed by an Acton Research single 0.5-m focal length grating spectrograph (600 g/mm with 1-µm blaze) and detected by an Andor iDus InGaAs linear photodiode array. Time-resolved µ-PL (µ-TRPL) experiments were performed with a PicoQuant 790-nm semiconductor pulsed diode (pulse width, <100 ps) working at a repetition rate of 10 MHz. In this case, dispersed signal by the same monochromator was collected by an InGaAs APD (model id230 from idQuantique) working in Geiger mode with 10-Hz dark counts and a timing resolution of 200 ps that was attached to a time-correlated single photon counting electronic board (TCC900 from Edinburgh Instruments). The experimental time resolution by deconvolution was estimated to be around 50 ps. Simultaneous PL and TRPL spectra at visible wavelengths (400 to 1000 nm) were measured by a similar experiment using a 200-fs pulsed Ti:Sapphire (Coherent Mira 900D) at a repetition rate of 76 MHz doubled to 400 nm with a BBO crystal. The PL signal was dispersed by an Acton Research double 0.3-m focal length grating spectrograph and detected by an Andor Newton 970 electron multiplying CCD camera in the case of PL and by a Si micro photon device single-photon avalanche diode photodetector in the case of TRPL. Additional complementary PL experiments were performed by using a continuous wave GaN laser (405 nm), a 533-nm DSPP (diode pumped solid state) laser, or a 780-nm semiconductor diode and detecting the backscattered PL by Ocean Optics HR4800/NIRQuest512 spectrographs at visible/IR wavelengths.

SUPPLEMENTARY MATERIALS

Supplementary material for this article is available at http://advances.sciencemag.org/cgi/content/full/2/1/e1501104/DC1

Fig. S1. SEM picture of the surfaces of the different layers.
Fig. S2. Normalized PL for QDs in solution, on film, and on film after the ligand exchange.
Fig. S3. PL of PS single layer and PS/QD and QD/PS using 2.3 nm.
Fig. S4. Energy band position of PS and QD conduction and VB extracted from literature.
Fig. S5. Comparison of the exciplex PL for QD/PS and PS/QD samples with 2.3-nm QDs.
Fig. S6. Comparison between PS/QD and QD/PS configurations for 3-nm QDs.
Fig. S7. Analysis of PL excitation measurement and estimation of the hole transfer time from PS into QD.
Fig. S8. Current-potential curve for prepared QDs.
Fig. S9. Normalized EL for PS, QD, and QD/PS.
Fig. S10. EL at different applied biases for PS/QD configuration using both 2.3- and 3-nm QDs.
Fig. S11. EQE of the different LEDs prepared.

REFERENCES AND NOTES

1. W. S. Yang, J. H. Noh, N. J. Jeon, Y. C. Kim, S. Ryu, J. Seo, S. I. Seok, High-performance photovoltaic perovskite layers fabricated through intramolecular exchange. *Science* **348**, 1234–1237 (2015).
2. A. Kojima, K. Teshima, Y. Shirai, T. Miyasaka, Organometal halide perovskites as visible-light sensitizers for photovoltaic cells. *J. Am. Chem. Soc.* **131**, 6050–6051 (2009).
3. M. M. Lee, J. Teuscher, T. Miyasaka, T. N. Murakami, H. J. Snaith, Efficient hybrid solar cells based on meso-superstructured organometal halide perovskites. *Science* **338**, 643–647 (2012).
4. H.-S. Kim, C.-R. Lee, J.-H. Im, K.-B. Lee, T. Moehl, A. Marchioro, S.-J. Moon, R. Humphry-Baker, J.-H. Yum, J. E. Moser, M. Grätzel, N.-G. Park, Lead iodide perovskite sensitized all-solid-state submicron thin film mesoscopic solar cell with efficiency exceeding 9%. *Sci. Rep.* **2**, 591 (2012).
5. F. Deschler, M. Price, S. Pathak, L. E. Klintberg, D.-D. Jarausch, R. Higler, S. Hüttner, T. Leijtens, S. D. Stranks, H. J. Snaith, M. Atatüre, R. T. Phillips, R. H. Friend, High photoluminescence efficiency and optically pumped lasing in solution-processed mixed halide perovskite semiconductors. *J. Phys. Chem. Lett.* **5**, 1421–1426 (2014).

6. Y.-H. Kim, H. Cho, J. H. Heo, T.-S. Kim, N. Myoung, C.-L. Lee, S. H. Im, T.-W. Lee, Multicolored organic/inorganic hybrid perovskite light-emitting diodes. *Adv. Mater.* **27**, 1248–1254 (2015).
7. O. A. Jaramillo-Quintero, R. S. Sanchez, M. Rincon, I. Mora-Sero, Bright visible-infrared light emitting diodes based on hybrid halide perovskite with Spiro-OMeTAD as a hole-injecting layer. *J. Phys. Chem. Lett.* **6**, 1883–1890 (2015).
8. Z.-K. Tan, R. Saberi Moghaddam, M. Ling Lai, P. Docampo, R. Higler, F. Deschler, M. Price, A. Sadhanala, L. M. Pazos, D. Credgington, F. Hanusch, T. Bein, H. J. Snaith, R. H. Friend, Bright light-emitting diodes based on organometal halide perovskite. *Nat. Nanotechnol.* **9**, 687–692 (2014).
9. G. Xing, N. Mathews, S. S. Lim, N. Yantara, X. Liu, D. Sabba, M. Grätzel, S. Mhaisalkar, T. C. Sum, Low-temperature solution-processed wavelength-tunable perovskites for lasing. *Nat. Mater.* **13**, 476–480 (2014).
10. H. Zhu, Y. Fu, F. Meng, X. Wu, Z. Gong, Q. Ding, M. V. Gustafsson, M. T. Trinh, S. Jin, X.-Y. Zhu, Lead halide perovskite nanowire lasers with low lasing thresholds and high quality factors. *Nat. Mater.* **14**, 636–642 (2015).
11. S. Kazim, M. K. Nazeeruddin, M. Grätzel, S. Ahmad, Perovskite as light harvester: A game changer in photovoltaics. *Angew. Chem. Int. Ed.* **53**, 2812–2824 (2014).
12. A. P. Alivisatos, Semiconductor clusters, nanocrystals, and quantum dots. *Science* **271**, 933–937 (1996).
13. G. H. Carey, A. L. Abdelhady, Z. Ning, S. M. Thon, O. M. Bakr, E. H. Sargent, Colloidal quantum dot solar cells. *Chem. Rev.* **115**, 12732–12763 (2015).
14. K. Zhao, Z. Pan, I. Mora-Seró, E. Cánovas, H. Wang, Y. Song, X. Gong, J. Wang, M. Bonn, J. Bisquert, X. Zhong, Boosting power conversion efficiencies of quantum-dot-sensitized solar cells beyond 8% by recombination control. *J. Am. Chem. Soc.* **137**, 5602–5609 (2015).
15. Y. Shirasaki, G. J. Supran, M. G. Bawendi, V. Bulović, Emergence of colloidal quantum-dot light-emitting technologies. *Nat. Photonics* **7**, 13–23 (2013).
16. G. Seo, J. Seo, S. Ryu, W. Yin, T. K. Ahn, S. I. Seok, Enhancing the performance of sensitized solar cells with $PbS/CH_3NH_3PbI_3$ core/shell quantum dots. *J. Phys. Chem. Lett.* **5**, 2015–2020 (2014).
17. D. N. Dirin, S. Dreyfuss, M. I. Bodnarchuk, G. Nedelcu, P. Papagiorgis, G. Itskos, M. V. Kovalenko, Lead halide perovskites and other metal halide complexes as inorganic capping ligands for colloidal nanocrystals. *J. Am. Chem. Soc.* **136**, 6550–6553 (2014).
18. Z. Ning, X. Gong, R. Comin, G. Walters, F. Fan, O. Voznyy, E. Yassitepe, A. Buin, S. Hoogland, E. H. Sargent, Quantum-dot-in-perovskite solids. *Nature* **523**, 324–328 (2015).
19. A. Luque, A. Martí, Increasing the efficiency of ideal solar cells by photon induced transitions at intermediate levels. *Phys. Rev. Lett.* **78**, 5014–5017 (1997).
20. A. Luque, A. Martí, C. Stanley, Understanding intermediate-band solar cells. *Nat. Photonics* **6**, 146–152 (2012).
21. R. S. Sanchez, E. Binetti, J. A. Torre, G. Garcia-Belmonte, M. Striccolib, I. Mora-Sero, All solution processed low turn-on voltage near infrared LEDs based on core–shell PbS–CdS quantum dots with inverted device structure. *Nanoscale* **6**, 8551–8555 (2014).
22. A. G. Pattantyus-Abraham, I. J. Kramer, A. R. Barkhouse, X. Wang, G. Konstantatos, R. Debnath, L. Levina, I. Raabe, M. K. Nazeeruddin, M. Grätzel, E. H. Sargent, Depleted-heterojunction colloidal quantum dot solar cells. *ACS Nano* **4**, 3374–3380 (2010).
23. P. R. Brown, D. Kim, R. R. Lunt, N. Zhao, M. G. Bawendi, J. C. Grossman, V. Bulović, Energy level modification in lead sulfide quantum dot thin films through ligand exchange. *ACS Nano* **8**, 5863–5872 (2014).
24. G. D. Scholes, M. Jones, S. Kumar, Energetics of photoinduced electron-transfer reactions decided by quantum confinement. *J. Phys. Chem. C* **111**, 13777–13785 (2007).
25. J. J. Benson-Smith, J. Wilson, C. Dyer-Smith, K. Mouri, S. Yamaguchi, H. Murata, J. Nelson, Long-lived exciplex formation and delayed exciton emission in bulk heterojunction blends of silole derivative and polyfluorene copolymer: The role of morphology on exciplex formation and charge separation. *J. Phys. Chem. B* **113**, 7794–7799 (2009).
26. V. D'Innocenzo, A. R. Srimath Kandada, M. De Bastiani, M. Gandini, A. Petrozza, Tuning the light emission properties by band gap engineering in hybrid lead halide perovskite. *J. Am. Chem. Soc.* **136**, 17730–17733 (2014).
27. A. Listorti, E. J. Juarez-Perez, C. Frontera, V. Roiati, L. Garcia-Andrade, S. Colella, A. Rizzo, P. Ortiz, I. Mora-Sero, Effect of mesostructured layer upon crystalline properties and device performance on perovskite solar cells. *J. Phys. Chem. Lett.* **6**, 1628–1637 (2015).
28. P. Moroz, N. Kholmicheva, B. Mellott, G. Liyanage, U. Rijal, E. Bastola, K. Huband, E. Khon, K. McBride, M. Zamkov, Suppressed carrier scattering in CdS-encapsulated PbS nanocrystal films. *ACS Nano* **7**, 6964–6977 (2013).
29. B. Chastaingt, M. Gurioli, P. Borri, M. Colocci, G. Neu, C. Deparis, J. Massies, J. Martinez-Pastor, Controlled type-I–type-II transition in $GaAs/AlAs/Al_xGa_{1-x}as$ double-barrier quantum wells. *Phys. Rev. B* **55**, 2393 (1997).
30. L. Gil-Escrig, G. Longo, A. Pertegás, C. Roldán-Carmona, A. Soriano, M. Sessolo, H. J. Bolink, Efficient photovoltaic and electroluminescent perovskite devices. *Chem. Commun.* **51**, 569–571 (2015).
31. A. Martí, C. R. Stanley, C. D. Farmer, N. López, P. Díaz, E. Cánovas, P. G. Linares, A. Luque, Production of photocurrent due to intermediate-to-conduction-band transitions: A demonstration of a key operating principle of the intermediate-band solar cell. *Phys. Rev. Lett.* **97**, 247701 (2006).
32. S. A. Blokhin, A. V. Sakharov, A. M. Nadtochy, A. S. Pauysov, M. V. Maximov, N. N. Ledentsov, A. R. Kovsh, S. S. Mikhrin, V. M. Lantratov, S. A. Mintairov, N. A. Kaluzhniy, M. Z. Shvarts, AlGaAs/GaAs photovoltaic cells with an array of InGaAs QDs. *Semiconductors* **43**, 514–518 (2009).
33. W.-J. Yin, T. Shi, Y. Yan, Unique properties of halide perovskites as possible origins of the superior solar cell performance. *Adv. Mater.* **26**, 4653–4658 (2014).

Acknowledgments: We would like to acknowledge SCSCIE from the University of Valencia–Estudi General and especially E. Navarro Raga for his help in the SEM and EDX measurements. I.M-S. would like to thank J. Planelles and J. I. Climente for the fruitful discussion about the topics of this paper. **Funding:** This work was supported by Generalitat Valenciana (projects PROMETEOII/2014/NNN, PROMETEOII/2014/059, and ISIC/2012/008), the Universitat Jaume I (project 12I361.01/1), and Spanish MINECO (Ministry of Economy and Competitiveness; projects MAT2013-47192-C3-1-R and TEC2014-53727-C2-1-R). M.S.F. would like to thank CONACYT México for its postdoctoral grant. **Author contributions:** I.M.-S. conceived the work and design experiments. R.S.S. and I.M.-S. designed the sample configuration. R.S.S. and M.S.F. prepared the QDs and produced all the samples analyzed. R.S.S., M.S.F., and I.S. measured PL and EL of the samples. M.S.F. and I.S. performed SEM and EDX characterization. J.P.M.-P. and I.S. designed the excitation PL spectra and PL transient experiments. I.S. and G.M.-M. measured the excitation PL spectra and PL transient. J.P.M.-P. and I.M.-S. led all the work. I.M.-S. wrote the first version of the manuscript, and all authors contributed to the final version. **Competing interests:** The authors declare that they have no competing interests. **Data and materials availability:** All data needed to evaluate the conclusions in the paper are present in the paper and/or the Supplementary Materials. Additional data related to this paper are available from the authors upon request. Requests for data and materials should be addressed to I.M.-S. (sero@uji.es).

Submitted 14 August 2015
Accepted 19 November 2015
Published 22 January 2016
10.1126/sciadv.1501104

Citation: R. S. Sanchez, M. S. de la Fuente, I. Suarez, G. Muñoz-Matutano, J. P. Martinez-Pastor, I. Mora-Sero, Tunable light emission by exciplex state formation between hybrid halide perovskite and core/shell quantum dots: Implications in advanced LEDs and photovoltaics. *Sci. Adv.* **2**, e1501104 (2016).

Science Advances

Tunable light emission by exciplex state formation between hybrid halide perovskite and core/shell quantum dots: Implications in advanced LEDs and photovoltaics

Rafael S. Sanchez, Mauricio Solis de la Fuente, Isaac Suarez, Guillermo Muñoz-Matutano, Juan P. Martinez-Pastor and Ivan Mora-Sero

Sci Adv **2** (1), e1501104.
DOI: 10.1126/sciadv.1501104